Constructing a MoS$_2$ QDs/CdS Core/Shell Flowerlike Nanosphere Hierarchical Heterostructure for the Enhanced Stability and Photocatalytic Activity

Shijing Liang [1,2,3,*], **Zhouming Zhou** [2], **Xiuqin Wu** [2], **Shuying Zhu** [1], **Jinhong Bi** [1,2], **Limin Zhou** [3], **Minghua Liu** [1,2] **and Ling Wu** [1]

1   State Key Laboratory of Photocatalysis on Energy and Environment, Fuzhou University, Fuzhou 350002, China; liangzhu-2015@outlook.com (S.Z.); bijinhong@fzu.edu.cn (J.B.); mhliu2000@fzu.edu.cn (M.L.); wuling@fzu.edu.cn (L.W.)
2   Department of Environmental Science and Engineering, College of Environment and Resource Fuzhou University, Minhou, Fujian 350108, China; fdzhouzming@163.com (Z.Z.); wxqbelieve@163.com (X.W.)
3   Department of Mechanical Engineering, The Hong Kong Polytechnic University, Hung Hom, Kowloon, Hong Kong, China; mmlmzhou@polyu.edu.hk
*   Correspondence: sjliang2011@gmail.com; Tel.: +86-591-22866070

Abstract: MoS$_2$ quantum dots (QDs)/CdS core/shell nanospheres with a hierarchical heterostructure have been prepared by a simple microwave hydrothermal method. The as-prepared samples are characterized by XRD, TEM, SEM, UV-VIS diffuse reflectance spectra (DRS) and N$_2$-sorption in detail. The photocatalytic activities of the samples are evaluated by water splitting into hydrogen. Results show that the as-prepared MoS$_2$ QDs/CdS core/shell nanospheres with a diameter of about 300 nm are composed of the shell of CdS nanorods and the core of MoS$_2$ QDs. For the photocatalytic reaction, the samples exhibit a high stability of the photocatalytic activity and a much higher hydrogen evolution rate than the pure CdS, the composite prepared by a physical mixture, and the Pt-loaded CdS sample. In addition, the stability of CdS has also been greatly enhanced. The effect of the reaction time on the formations of nanospheres, the photoelectric properties and the photocatalytic activities of the samples has been investigated. Finally, a possible photocatalytic reaction process has also been proposed.

Keywords: MoS$_2$ QDs; CdS-based composite; core-shell structure; photocatalysis; water splitting

1. Introduction

In recent years, photocatalytic technology has been extensively used for producing H$_2$ utilizing solar energy. However, typical TiO$_2$ photocatalyst solely absorbs UV light, which is only about 4% of the entire solar spectrum. In view of the efficient utilization of visible light, developing suitable and novel photocatalysts, which work efficiently under a wide range of visible light irradiation conditions, is a very hot topic [1,2].

Among the various reported photocatalysts [3–10], metal sulfides are regarded as excellent candidates for visible light-driven photocatalysis because of their suitable band gap and high catalytic activity. In particular, CdS is the most famous photocatalyst with a band gap value of 2.4 eV, and its conduction band position is more negative than the H$_2$O/H$_2$ reduction potential [11,12]. However, there are several issues that still limit the photocatalytically-reductive activity of pure CdS particles. For example, CdS particles tend to aggregate and form larger particles, which result in a reduced surface area and a higher recombination rate of the photogenerated electron-hole

pairs [11]. Another serious drawback of CdS photocatalysts is the problem of photocorrosion [13,14]. The sulfide anion can be easily oxidized by photogenerated holes. This photocorrosion effect leads to most CdS structures being highly unstable as photocatalysts and, thus, limits their practical application [15,16]. To solve these problems, many approaches have been proposed to enhance the photoreductive activity and photostability of CdS, like preparing quantized CdS nanocrystallites, designing controllable morphologies, depositing noble metals, preparing colloidal CdS and forming CdS-based composites. Numerous nanostructured CdS photocatalysts with controllable morphologies have been synthesized [17–23], such as nanospheres, nanorods, flowers, nanotubes, nanocubes, petals and nanobelts. All of these nanostructured CdS photocatalysts shows higher hydrogen production activity than the bulk CdS, but the problem of photocorrosion was still serious.

Cocatalysts can offer the low activation potentials for H_2 or O_2 evolution and act as active sites for H_2 or O_2 formation, so it is crucial for photocatalytic H_2 production reactions [24–28]. Cocatalysts are capable of assisting in electron-hole separation at the cocatalyst/semiconductor interface; thus, it may significantly inhibit the photocorrosion effect. Among the developed low-cost cocatalysts, MoS_2, which is composed of Mo atoms sandwiched between two layers of hexagonal closely-packed sulfur atoms, has been extensively investigated [29,30]. It is reported that MoS_2 is an efficient co-catalyst when coupled with semiconductors, such as TiO_2 [31,32], CdS [27] and g-C_3N_4 [28], having shown remarkable enhancement in H_2 evolution and the degradation of pollutants. In contrast to the widely-used Pt particle co-catalyst, the various morphologies of MoS_2 can be easily controlled by using hydrothermal methods or high temperature processes under H_2S atmosphere. These MoS_2 structures showed high co-catalytic activities for hydrogen evolution [32,33]. However, the obtained MoS_2 nanostructures are usually formed of irregular aggregates of nanoparticles or stacked multilayers deposited on a substrate; this problem also inhibits the co-catalytic activities for hydrogen evolution. Therefore, up to now, our knowledge regarding how to design or fabricate efficient MoS_2/CdS nanocomposites is far from satisfactory.

In this work, MoS_2 quantum dots (QDs) were prepared by a photo-assisted chemical etching method for the first time, and then, noble metal-free flowerlike MoS_2 QDs/CdS core/shell nanosphere photocatalysts were synthesized by a one-pot microwave hydrothermal route. The physicochemical properties of the as-prepared samples were characterized in detail. The possible formation of flowerlike nanospheres was also proposed. The photocatalytic activities of the samples were evaluated by water splitting into hydrogen under visible light irradiation. Furthermore, the probable influencing factors for the enhanced stability and activity of CdS have also been investigated.

2. Results and Discussion

2.1. Phase Structure and Morphology

The crystalline phase of MoS_2 quantum dots (QDs) was analysis using the dried MoS_2 QDs (Figure S1 in supplementary material). The diffraction peaks of the as-prepared MoS_2 correspond well to the hexagonal phases of MoS_2 (JCPDS Card No. 77-1716). The morphology of MoS_2 QDs was determined by a TEM technique. It could be found that the sizes of MoS_2 QDs were less than 10 nm and have a narrow size distribution with high dispersity in aqueous solution (Figure S2). Figure 1 shows the X-ray diffraction patterns of CdS and MoS_2 QDs/CdS prepared by a microwave-hydrothermal reaction for 1 h. Diffraction peaks correspond well to the hexagonal phases of CdS (JCPDS Card No. 70-2553). Significantly, the XRD pattern of the MoS_2 QDs/CdS composites shows that no impurity peaks could be detected from the XRD measurements. Notably, the diffraction peaks assigned to MoS_2 are not observed over the MoS_2 QDs/CdS sample; this is possible due to the low amount of MoS_2 QDs loaded on CdS [34].
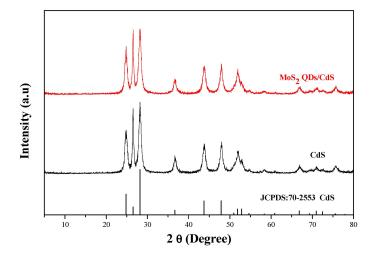
Figure 1. XRD patterns of the as-prepared CdS and MoS$_2$ QDs-CdS.

The samples were further characterized by TEM and SEM techniques to investigate the morphologies and the interfacial structures between MoS$_2$ and CdS. As shown in Figure 2, the CdS prepared using L-cysteine as the S resource exhibits a monodispersed and uniform nanorod structure with a length of 100 nm and 10 nm in lateral size. The morphology is also confirmed by the SEM images, as shown in Figure S3. For the MoS$_2$ QDs/CdS sample prepared for 1 h, it can be seen clearly that it shows a monodispersed and uniform flowerlike nanosphere structure with a size of 300 nm (Figure S4). From TEM images (Figure 2b,c), the nanosphere with hierarchical structures is constructed by many nanorods. The length of the nanorods is about 300 nm, and their width is about 20 nm. The HRTEM image shows the sample with high crystallinity. The space value of the clear lattice fringes (d = 0.21 nm) matches well with that of the (104) planes of the CdS crystal, indicating that the composition of the nanorod is CdS. Furthermore, we could also conclude that the nanorods grow along the [104] crystal plane.
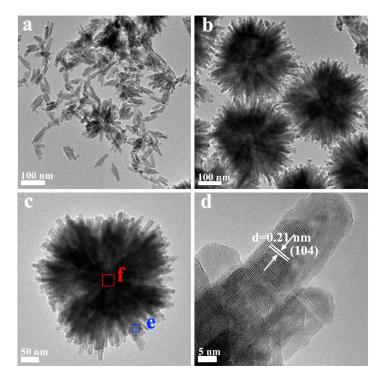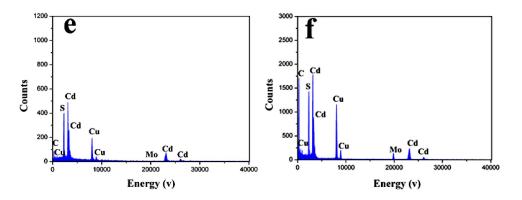

Figure 2. *Cont.*

Figure 2. TEM images of pure CdS (**a**) and MoS$_2$ QDs/CdS (**b,c**), HRTEM image of CdS MoS$_2$ QDs/CdS (**d**) and EDS images (**e,f**) in the e and f areas of Figure 2c.

Energy dispersive X-ray spectrometry (EDS) mapping analysis of the MoS$_2$ QDs/CdS nanospheres was used to confirm the distribution of the Cd, Mo and S elements. As shown in Figure 2e, Cd and S elements were only found, but not Mo elements in the **e** area of Figure 2c. The Cu and C peaks in the spectra are derived from a carbon-coated copper TEM grid. However, in Figure 2f, Cd, S and Mo elements have been found in the **f** area of Figure 2c. Thus, it can be concluded that MoS$_2$ is in the central portion of the nanoflower, but not on the nanorod. The MoS$_2$ QDs/CdS nanospheres are a core/shell hetero-structure. MoS$_2$ serves as the crystal nucleus for the growth of CdS nanorods. Notably, due to the direct growth of CdS nanorods on the MoS$_2$, the interaction between MoS$_2$ and CdS would be very strong. The excellent interfacial interaction between CdS and MoS$_2$ is expected to improve the separation of photogenerated charge carriers, and therefore, the photocatalytic activity would be enhanced. The percentage of Mo element content is also evaluated to be about 0.1%.

2.2. The Possible Formation Process of the Flowerlike Nanospheres

In order to find the possible formation process of the nanospheres, the samples were also prepared by the microwave-hydrothermal reaction for 5 min, 15 min and 30 min at 180 °C. Figure 3a shows that the sample prepared for 5 min was constructed by the nanosphere and the irregular aggregates. From the XRD result (Figure S5), we could see that the sample is composed of crystalline CdS and intermediate products, although the crystallinity of the sample is poor. Prolonging the reaction time (Figure 3b,c), the part of the irregular aggregates is reduced, and the nanorods grow gradually. XRD result also shows the intermediate products disappear gradually, and the crystallinity of the sample is enhanced. When the samples were prepared for 1 h (Figure 3d), a monodispersed nanosphere composed of nanorods is obtained, and no irregular aggregates are observed. On the basis of the above experiment results, the morphological evolution mechanism of hierarchical flowerlike MoS$_2$ QDs/CdS core/shell nanospheres can be proposed in following steps: (i) nucleation of irregular aggregates nanosphere and some intermediate products; (ii) dissolution-recrystallization growth; (iii) further growth and monodispersed nanospheres composed of nanorods are obtained. This may suggest that the reaction proceeds as a dissolution-recrystallization process [35–37]. As a comparison, MoS$_2$ QDs-L-cys was replaced by MoS$_2$ QDs during the microwave hydrothermal reaction process. It can be seen that flowerlike nanospheres were also formed. However, some large particles were also yielded, and the nanospheres exhibited a serious accumulation (Figure S6). That is, the MoS$_2$ QDs play the role of the crystal nucleus for the growth of the nanosphere. L-cysteine not only serves as the S resource, but also facilitates the dispersion of nanosphere during the formation process. The possible formation process is schematically illustrated in Figure 4.
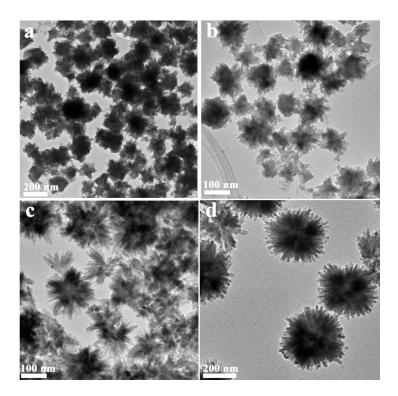
Figure 3. TEM images of the MoS$_2$ QDs/CdS samples prepared for different times: (**a**) 5 min; (**b**) 15 min; (**c**) 30 min; (**d**) 60 min.
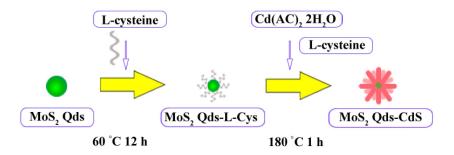

Figure 4. Schematic illustration of the formation process of the MoS$_2$ QDs/CdS nanoflower.

2.3. Photocatalytic Properties

Figure 5 shows that the as-prepared samples exhibit a clear activity for the water splitting into H$_2$. The amount of H$_2$ evolution on pure CdS is 8.07 μmol after reaction for four hours, corresponding to about 100 μmol·h^{-1}·g^{-1} of the H$_2$ evolution rate. However, the activity of the MoS$_2$ QDs/CdS sample could reach to 25.02 μmol after four hours and the H$_2$ evolution rate is 312.75 μmol·h^{-1}·g^{-1}, which is over three-times higher than that of pure CdS. This may be owed to flowerlike hierarchical heterostructure morphology, and MoS$_2$ QDs serve as the co-catalyst to facilitate the separation of photogenerated electron and hole pairs. The photocatalytic activities of MoS$_2$ QDs/CdS samples are sensitive to the reaction time. With prolonging the reaction time, the activity is increased. The sample prepared for a short time may possess abundant defects to act at the recombination sites for the photogenerated electron and hole to reduce the activity. Furthermore, the 1D CdS nanorods could also promote the transfer of photogenerated electron and hole. This may be another reason for the enhanced photocatalytic activity. The MoS$_2$ QDs/CdS sample prepared for 5 min exhibited the lowest H$_2$ evolution rate (66.5 μmol·h^{-1}·g^{-1}), which may be due to the poor crystallinity and the existence of the intermediate products.
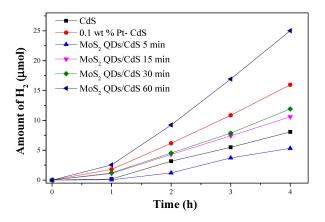
Figure 5. The amount of H_2 evolution on CdS, MoS_2 QDs/CdS (5 min,15 min,30 min 60 min), 0.1 wt % Pt-CdS catalysts under visible light irradiation (reaction conditions: 20 mg catalysts, 45 mL H_2O containing 5 mL 0.02 M NaS and 0.025 M $NaSO_3$, $\lambda > 420$ nm).

Pt was demonstrated to be the most promising cocatalyst for H_2 evolution. As a comparison, the same content of Pt (0.1 wt %) was photodeposited on the as-prepared photocatalysts by directly dissolving H_2PtCl_6 (10 mg/L) into the reactant suspension. The activities of the CdS catalysts are increased from 100 to 199.5 $\mu mol \cdot h^{-1} \cdot g^{-1}$ after Pt loading. It should be pointed out that this H_2 evolution rate is still lower than that of the corresponding MoS_2 QDs/CdS sample. The results clearly indicate that MoS_2 QDs could function as a more efficient co-catalyst for CdS photocatalyst compared to Pt. Furthermore, some controlled experiments have also been carried out. As shown in Figure S7, MoS_2 QDs could not produce hydrogen under visible light irradiation. That is, the role of MoS_2 QDs is as the cocatalyst. The sample (denoted as MoS_2 QDs + CdS) was also prepared by a mechanical mixture of MoS_2 QDs and CdS nanorods as a reference. It is found that MoS_2 QDs + CdS exhibits a superior activity compared to pure CdS. However, the activity of this sample is much lower than that of the MoS_2 QDs/CdS sample.

The stability of the samples was also studied under visible light irradiation. As shown in Figure 6, no obvious loss activity has been observed over the MoS_2 QDs/CdS sample. However, the hydrogen evolution rate of pure CdS shows a significant decrease during the photocatalytic water splitting process. All of the results indicate that MoS_2 QDs could inhibit the photocorrosion of CdS.
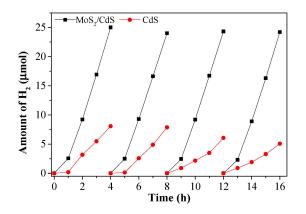

Figure 6. The stability of the activity over CdS and MoS_2 QDs/CdS under visible light irradiation (reaction conditions: 20 mg catalysts, 45 mL H_2O containing 5 mL 0.02 M NaS and 0.025 M $NaSO_3$, $\lambda > 420$ nm).

2.4. Photoabsorption Performance and BET Surface Area

As the photoabsorption properties play a crucial role in determining the photocatalytic activity, the UV-VIS diffuse reflectance spectra of the samples were recorded (Figure 7). Obviously, the samples have a strong absorption in the visible light region. The pure CdS sample has an absorption edge at 516 nm, corresponding to the energy value of 2.40 eV [38]. The absorption edge of MoS_2 QDs/CdS has a small blue-shift, which is located at 510 nm. This small blue-shift may be due to the strong interaction between MoS_2 and CdS. No clear absorption has been observed in the range of 550 to 800 nm, further indicating that no MoS_2 QDs load on the shell of the nanosphere. It is worth noting that the absorption capacity of MoS_2 QDs/CdS is higher than that of pure CdS in the range of 400 to 470 nm. The sample absorbing more photons with high energy will produce more electrons with a high reduction ability to reduce the water molecules. Thus, the sample may exhibit a high hydrogen evolution rate.
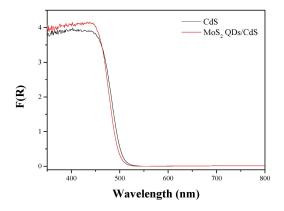

Figure 7. UV-VIS diffuse reflectance spectra (DRS) of CdS and MoS_2 QDs/CdS.

The nitrogen adsorption-desorption isotherms of CdS and MoS_2 Qds-CdS reveal that all of the samples exhibit a Type IV adsorption-desorption isotherm with a H_3 hysteresis loop in the relative pressure range of 0.6 to 1.0 (Figure 8), indicating the presence of mesopores [38,39]. These mesopores may originate from the accumulation of CdS nanorods in the nanospheres. In addition, the BET specific surface area, pore volume, average pore size and H_2 production rate of the samples are summarized in Table 1. The surface area, pore volume and average pore size of MoS_2 QDs/CdS are larger than those of pure CdS. Generally, a larger BET surface area could provide more reaction sites for the photocatalytic reaction [40]. A large pore size and mesopores structures could facilitate the contact between the photocatalyst and reactants, as well as the mass transfer. Therefore, these may be one of the reasons for the enhanced H_2 evolution activity.
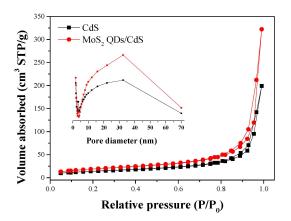

Figure 8. Nitrogen adsorption-desorption isotherms and the corresponding pore-size distribution curves (inset) for the CdS and MoS_2 QDs/CdS.

Table 1. The BET surface area, pore volume, average pore size and H_2 evolution rate of the samples.

Sample	Surface Area $(m^2 \cdot g^{-1})$	Pore Volume $(cm^3 \cdot g^{-1})$	Average Pore Size (nm)	H_2 Evolution Rate $(\mu mol \cdot h^{-1} \cdot g^{-1})$
CdS	50.7	10.3	25.13	100.8
MoS_2 QDs/CdS	68.97	10.49	29.67	312.75

2.5. Photoelectrochemical Performance

To investigate the electron generation and the charge carrier transport characteristics of the as-prepared samples, the transient photocurrent responses of CdS and MoS_2 QDs/CdS heterostructure electrodes were recorded over several on-off cycles under visible light irradiation. As shown in Figure 9, it could be found that the photocurrent value rapidly decreases to the initial value as soon as the irradiation of light was off, and the photocurrent comes back to a constant value when the light is on again. It could be seen that the CdS and MoS_2 Qds-CdS electrodes have a steady photoelectrochemical performance under visible light irradiation ($\lambda > 420$ nm). Notably, the photocurrent intensity of MoS_2 QDs/CdS is four-fold higher than that of the pure CdS. The results may show the MoS_2 QDs/CdS sample with the higher e-h$^+$ separation efficiency under visible light irradiation [41]. Therefore, a higher photocatalytic activity would be achieved. Moreover, the MoS_2 Qds-CdS electrode photocurrent value decreased more slowly than the CdS electrode to the initial value when the irradiation of light is off, which suggests the low e-h$^+$ recombination rate [42]. These photoelectrochemical performance results are in accord with the aforementioned photocatalytic H_2 production activity.
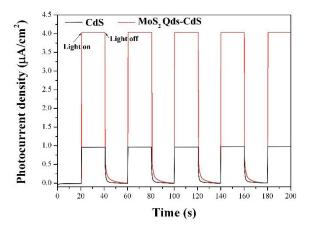

Figure 9. Transient photocurrent density *versus* time plotted for CdS and MoS_2 QDs/CdS in 0.2 M Na_2SO_4 electrolyte under visible light irradiation.

2.6. Possible Photocatalytic Mechanism

On the basis of the results and discussions of the aforementioned experiments, the improved photocatalytic activities and inhibition of CdS corrosion of flowerlike MoS_2 QDs/CdS composites may be attributed to the hierarchical heterostructure morphology, the fast charge separation and the slow charge carrier recombination. A probable mechanism for the photocatalytic hydrogen production process is proposed, as illustrated in Figure 10. Under visible light irradiation, the CdS nanorods are excited to generate charge carriers. The photogenerated electrons and holes of CdS can transfer quickly in the 1D nanorod structure to MoS_2 QDs, owing to their intimate interfacial contact and matched band position. Due to the strong quantum confinement and edge effects of MoS_2 QDs, they can act as an efficient cocatalyst to provide active sites with low overpotential for hydrogen production. For the other band, the hole will transfer to the other side to react with the sacrifice agent (S^{2-}), which will suppress the corrosion of CdS. Furthermore, the mesostructure formed by the

accumulation of nanorods could reflect the incident light multiple times, resulting in the improved light harvesting ability.
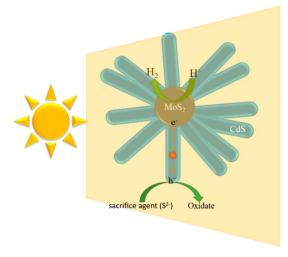

Figure 10. Schematic of photogenerated charge transfer and photocatalytic reaction over the MoS_2 QDs/CdS under visible light irradiation.

3. Experimental Section

3.1. Synthesis of Photocatalysts

All chemical reagents were of analytical grade and purchased from Sinopharm Chemical Reagent Co. Ltd. (Shanghai, China) without further purification.

(1) Synthesis of MoS_2 QDs and MoS_2 QDs-Lcys: 50 mg commercial MoS_2 powder and 3 mL hydrogen peroxide (H_2O_2, 30 wt %) were added into 100 mL DI-water in a quartz tube under vigorous stirring at room temperature to ensure that the solution was fully mixed. Then, a light-grey suspension was obtained through UV light irradiation for 3 h. The resultant supernatant was centrifuged at 10,000 rpm for 15 min to separate the bulk MoS_2. Finally, the MoS_2 QDS suspension was formed. For the preparation of the MoS_2 QDs-Lcys precursor, 40 mg L-cysteine were added into 10 mL of the as-prepared MoS_2 QDS suspension under vigorous stirring.

(2) Synthesis of MoS_2 Qds–CdS: 1 mL of the MoS_2 Qds-Lcys suspension, 0.27 g of $Cd(Ac)_2 \cdot 2H_2O$ and 0.24 g of L-cysteine were dissolved in 30 mL of ethanolamine-water solution (volume ratio = 1:1) under magnetic stirring for 1 h. L-cysteine served as the S resource. The solution was then transferred into a Teflon-lined autoclave, which was placed in a microwave-hydrothermal synthesis system (ETHOS One, Milestone, Sorisole, Italy) and kept at 180 °C for a given time. After the reaction, the autoclave was cooled to room temperature, and the resulting precipitate was collected by centrifugation, alternately rinsed several times with distilled water and ethanol. The final product was dried in a vacuum oven at 80 °C over 12 h. The referenced CdS was also synthesized following the same process without the MoS_2 QDs suspension.

3.2. Characterization

The as-prepared samples were characterized by powder X-ray diffraction (XRD) on a Bruker D8 Advance X-ray diffractometer (Karlsruhe, Germany) operated at 40 kV and 40 mA with Ni-filtered Cu K_α irradiation (λ = 1.5406Å). Transmission electron microscopy (TEM) images were recorded using a JEOL model JEM 2010 EX microscope (Peabody, MA, USA) at an accelerating voltage of 200 kV. Scanning electron microscopy (SEM) images were obtained with a Nova NanoSEM 230 microscopy (FEI Corp., Hillsboro, OR, USA) UV-VIS diffuse reflectance spectra (UV-VIS DRS) were obtained by using a UV-VIS spectrophotometer (Varian Cary 500, Santa Clara, CA, USA), and the

data were converted to Kubelka-Munk (KM) functions. Barium sulfate was used as a reference. The Brunauer-Emmett-Teller (BET) surface area was measured with an ASAP2020M apparatus (Micromeritics Instrument Corp., Norcross, GA, USA).

3.3. Photoelectrochemical Measurements

The working electrode was prepared on fluorine-doped tin oxide (FTO) glass, which was cleaned by sonication in chloroform, acetone and ethanol for 30 min. The glass was then rinsed with pure water (18 MΩ cm) and dried in the air. The FTO slide was dip coated with 10 μL of slurry, which was obtained from mixture of 5 mg powder and 0.5 mL dimethylformamide under sonication for 2 h to get a thin film of the samples coated on the FTO slide. After air drying naturally, a copper wire was connected to the side part of the FTO glass using conductive tape. The uncoated parts of the electrode were isolated with an epoxy resin, and the exposed area of the electrode was 0.25 cm^2. The electrochemical measurements were performed in a conventional three-electrode cell, using a Pt plate and a saturated Ag/AgCl electrode as the counter electrode and reference electrode, respectively. The working electrodes were immersed in a 0.2 M Na_2SO_4 aqueous solution without any additive for 30 s before measurement. The photocurrent measurements were conducted with a CHI650E electrochemical workstation (Chenhua Instruments, Shanghai, China). A 300-W Xe lamp (Beijing Trustech, PLS-SXE300c, Beijing, China) with a 420-nm cut-off filter was used as a light source.

3.4. Photocatalytic Activity

The photocatalytic activities of MoS_2/CdS core/shell composites were evaluated by the decomposition of H_2O in an aqueous solution. The catalyst (20 mg) was suspended in a 45-mL Pyrex glass vessel, which contained 5 mL 0.02M NaS and 0.025 M $NaSO_3$ solutions. The light source was a 300-W Xe lamp (Beijing Trustech, PLS-SXE300c,) with a 420-nm cut-off filter. The temperature of the reactant solution was maintained at 275 K by a flow of cooling water during the reaction. The reaction solution was evacuated several times to remove air completely prior to irradiation. The amount of H_2 produced was analyzed using an online gas chromatography. Zero-point-one weight percent of Pt cocatalyst was photodeposited on the catalysts by directly dissolving H_2PtCl_6 (10 mg/L) into the reactant suspension, if necessary.

4. Conclusions

In conclusion, monodispersed MoS_2 QDs/CdS core/shell flowerlike nanospheres have been prepared by a microwave hydrothermal method. The as-prepared MoS_2 QDs/CdS samples exhibit superior photocatalytic activity compared to pure CdS, Pt/CdS and the composite prepared by a physical mixture. The hydrogen evolution rate of MoS_2 QDs/CdS could reach 312.75 $\mu mol \cdot h^{-1} \cdot g^{-1}$, which is over three-times that of CdS. Furthermore, the stability of CdS is greatly enhanced. The enhanced activity of CdS could be attributed to the unique morphology, the improved charge separation rate and the reduced charge recombination rate. Notably, MoS_2 QDs is more suitable as a cocatalyst for hydrogen evolution on CdS than the noble metal Pt in our experiments.

Author Contributions: Shijing Liang conceived of the project and supervised the research work. The experiments were mainly finished by Shijing Liang and Zhouming Zhou; part of the experiments were done by Xiuqin Wu and Shuying Zhu. The paper was revised by Jinhong Bi, Limin Zhou, Minghua Liu and Ling Wu, putting forward valuable opinions. All authors contributed to the discussions of the results and the paper writing.

Conflicts of Interest: The authors declare no conflict of interest.

References

1. Zheng, Y.; Lin, L.; Wang, B.; Wang, X. Graphitic carbon nitride polymers toward sustainable photoredox catalysis. *Angew. Chem. Int. Ed.* **2015**, *54*, 12868–12884. [CrossRef] [PubMed]
2. Ran, J.; Zhang, J.; Yu, J.; Jaroniec, M.; Qiao, S.Z. Earth-abundant cocatalysts for semiconductor-based photocatalytic water splitting. *Chem. Soc. Rev.* **2014**, *43*, 7787–7812. [CrossRef] [PubMed]
3. Shen, Z.; Sun, S.; Wang, W.; Liu, J.; Liu, Z.; Yu, J.C. A black-red phosphorus heterostructure for efficient visible-light-driven photocatalysis. *J. Mater. Chem. A* **2015**, *3*, 3285–3288. [CrossRef]
4. Liu, G.; Yu, J.C.; Lu, G.Q.; Cheng, H.M. Crystal facet engineering of semiconductor photocatalysts: Motivations, advances and unique properties. *Chem. Commun.* **2011**, *47*, 6763–6783. [CrossRef] [PubMed]
5. An, X.; Yu, J.C. Graphene-based photocatalytic composites. *RSC Adv.* **2011**, *1*, 1426–1434. [CrossRef]
6. Liu, Y.; Xiong, J.; Luo, S.; Liang, R.; Qin, N.; Liang, S.; Wu, L. Ultrathin $HNbWO_6$ nanosheets: Facile synthesis and enhanced hydrogen evolution performance from photocatalytic water splitting. *Chem. Commun.* **2015**, *51*, 15125–15128. [CrossRef] [PubMed]
7. Lin, Q.; Li, L.; Liang, S.; Liu, M.; Bi, J.; Wu, L. Efficient synthesis of monolayer carbon nitride 2D nanosheet with tunable concentration and enhanced visible-light photocatalytic activities. *Appl. Catal. B* **2015**, *163*, 135–142. [CrossRef]
8. Xiong, J.; Liu, Y.; Cao, C.; Shen, L.; Wu, W.; Liang, S.; Liang, R.; Wu, L. An architecture of $CdS/H_2Ti_5O_{11}$ ultrathin nanobelt for photocatalytic hydrogenation of 4-nitroaniline with highly efficient performance. *J. Mater. Chem. A* **2015**, *3*, 6935–6942. [CrossRef]
9. Liang, S.; Wen, L.; Lin, S.; Bi, J.; Feng, P.; Fu, X.; Wu, L. Monolayer HNb_3O_8 for selective photocatalytic oxidation of benzylic alcohols with visible light response. *Angew. Chem. Int. Ed.* **2014**, *53*, 2951–2955. [CrossRef] [PubMed]
10. Liang, S.; Zhu, S.; Chen, Y.; Wu, W.; Wang, X.; Wu, L. Rapid template-free synthesis and photocatalytic performance of visible light-activated $SnNb_2O_6$ nanosheet. *J. Mater. Chem.* **2012**, *22*, 2670–2678. [CrossRef]
11. Li, Q.; Li, X.; Wageh, S.; Al-Ghamdi, A.A.; Yu, J. CdS/Graphene Nanocomposite Photocatalysts. *Adv. Energy Mater.* **2015**, *5*. [CrossRef]
12. Zhai, T.; Fang, X.; Li, L.; Bando, Y.; Golberg, D. One-dimensional CdS nanostructures: Synthesis, properties, and applications. *Nanoscale* **2010**, *2*, 168–187. [CrossRef] [PubMed]
13. Xie, Y.P.; Yu, Z.B.; Liu, G.; Ma, X.L.; Cheng, H.M. CdS-mesoporous ZnS core-shell particles for efficient and stable photocatalytic hydrogen evolution under visible light. *Energy Environ. Sci.* **2014**, *7*, 1895–1901. [CrossRef]
14. Wu, K.; Chen, Z.; Lv, H.; Zhu, H.; Hill, C.L.; Lian, T. Hole removal rate limits photodriven H_2 generation efficiency in CdS-Pt and CdSe/CdS-Pt semiconductor nanorod–metal tip heterostructures. *J. Am. Chem. Soc.* **2014**, *136*, 7708–7716. [CrossRef] [PubMed]
15. Wu, L.; Yu, J.C.; Fu, X. Characterization and photocatalytic mechanism of nanosized CdS coupled TiO_2 nanocrystals under visible light irradiation. *J. Mol. Catal. A Chem.* **2006**, *244*, 25–32. [CrossRef]
16. Kudo, A.; Miseki, Y. Heterogeneous photocatalyst materials for water splitting. *Chem. Soc. Rev.* **2009**, *38*, 253–278. [CrossRef] [PubMed]
17. Jang, J.S.; Joshi, U.A.; Lee, J.S. Solvothermal synthesis of CdS nanowires for photocatalytic hydrogen and electricity production. *J. Phys. Chem. C* **2007**, *111*, 13280–13287. [CrossRef]
18. Xiang, Q.; Cheng, B.; Yu, J. Hierarchical porous CdS nanosheet-assembled flowers with enhanced visible-light photocatalytic H_2-production performance. *Appl. Catal. B* **2013**, *138–139*, 299–303. [CrossRef]
19. Chen, C.C.; Lin, J.J. Controlled growth of cubic cadmium sulfide nanoparticles using patterned self-assembled monolayers as a template. *Adv. Mater.* **2001**, *13*, 136–139. [CrossRef]
20. Li, L.; Wu, P.C.; Fang, X.S.; Zhai, T.Y.; Dai, L.; Liao, M.Y.; Koide, Y.; Wang, H.; Bando, Y.; Golberg, D. Single-crystalline CdS nanobelts for excellent field-emitters and ultrahigh quantum-efficiency photodetectors. *Adv. Mater.* **2010**, *22*, 3161–3165. [CrossRef] [PubMed]
21. Hu, Y.; Gao, X.H.; Yu, L.; Wang, Y.R.; Ning, J.Q.; Xu, S.J.; Lou, X.W. Carbon-coated CdS petalous nanostructures with enhanced photostability and photocatalytic activity. *Angew. Chem. Int. Ed. Engl.* **2013**, *25*, 5636–5639. [CrossRef] [PubMed]

22. Wang, C.Z.; Yifeng, E.F.; Fan, L.Z.; Wang, Z.H.; Liu, H.B.; Li, Y.L.; Yang, S.; Li, Y. Directed assembly of hierarchical CdS nanotube arrays from CdS nanoparticles: Enhanced solid state electro-chemiluminescence in H$_2$O$_2$ solution. *Adv. Mater.* **2007**, *19*, 3677–3681. [CrossRef]

23. Shen, L.; Liang, S.; Wu, W.; Liang, R.; Wu, L. CdS-decorated UiO-66(NH$_2$) nanocomposites fabricated by a facile photodeposition process: An efficient and stable visible-light-driven photocatalyst for selective oxidation of alcohols. *J. Mater. Chem. A* **2013**, *1*, 11473–11482. [CrossRef]

24. Yang, J.; Wang, D.; Han, H.; Li, C. Roles of Cocatalysts in photocatalysis and photoelectrocatalysis. *Acc. Chem. Res.* **2013**, *46*, 1900–1909. [CrossRef] [PubMed]

25. Zong, X.; Yan, H.; Wu, G.; Ma, G.; Wen, F.; Wang, L.; Li, C. Enhancement of photocatalytic H$_2$ evolution on CdS by loading MoS$_2$ as cocatalyst under visible light irradiation. *J. Am. Chem. Soc.* **2008**, *130*, 7176–7177. [CrossRef] [PubMed]

26. Xiang, Q.; Yu, J.; Jaroniec, M. Synergetic effect of MoS$_2$ and graphene as cocatalysts for enhanced photocatalytic H$_2$ production activity of TiO$_2$ nanoparticles. *J. Am. Chem. Soc.* **2012**, *134*, 6575–6578. [CrossRef] [PubMed]

27. Chang, K.; Li, M.; Wang, T.; Ouyang, S.; Li, P.; Liu, L.; Ye, J. Drastic layer-number-dependent activity enhancement in photocatalytic H$_2$ evolution over nMoS$_2$/CdS ($n \geqslant 1$) under visible light. *Adv. Energy Mater.* **2015**, *5*. [CrossRef]

28. Hou, Y.; Laursen, A.B.; Zhang, J.; Zhang, G.; Zhu, Y.; Wang, X.; Dahl, S.; Chorkendorff, I. Layered nanojunctions for hydrogen-evolution catalysis. *Angew. Chem. Int. Ed.* **2013**, *52*, 3621–3625. [CrossRef] [PubMed]

29. Xiong, J.; Liu, Y.; Wang, D.; Liang, S.; Wu, W.; Wu, L. An efficient cocatalyst of defect-decorated MoS$_2$ ultrathin nanoplates for the promotion of photocatalytic hydrogen evolution over CdS nanocrystal. *J. Mater. Chem. A* **2015**, *3*, 12631–12635. [CrossRef]

30. Xie, J.; Zhang, J.; Li, S.; Grote, F.; Zhang, X.; Zhang, H.; Wang, R.; Lei, Y.; Pan, B.; Xie, Y. Controllable disorder engineering in oxygen-incorporated MoS$_2$ ultrathin nanosheets for efficient hydrogen evolution. *J. Am. Chem. Soc.* **2013**, *135*, 17881–17888. [CrossRef] [PubMed]

31. Ho, W.; Yu, J.C.; Lin, J.; Yu, J.; Li, P. Preparation and photocatalytic behavior of MoS$_2$ and WS$_2$ nanocluster sensitized TiO$_2$. *Langmuir* **2004**, *20*, 5865–5869. [CrossRef]

32. Zhou, W.J.; Yin, Z.Y.; Du, Y.P.; Huang, X.; Zeng, Z.Y.; Fan, Z.X.; Liu, H.; Wang, J.Y.; Zhang, H. Synthesis of few-layer MoS$_2$ nanosheet-coated TiO$_2$ nanobelt heterostructures for enhanced photocatalytic activities. *Small* **2013**, *9*, 140–147. [CrossRef] [PubMed]

33. Chen, J.; Wu, X.-J.; Yin, L.; Li, B.; Hong, X.; Fan, Z.; Chen, B.; Xue, C.; Zhang, H. One-pot synthesis of CdS nanocrystals hybridized with single-layer transition-metal dichalcogenide nanosheets for efficient photocatalytic hydrogen evolution. *Angew. Chem. Int. Ed.* **2015**, *54*, 1210–1214. [CrossRef] [PubMed]

34. Zong, X.; Wu, G.P.; Yan, H.J.; Ma, G.J.; Shi, J.Y.; Wen, F.Y.; Wang, L.; Li, C. Photocatalytic H$_2$ evolution on MoS$_2$/CdS catalysts under visible light irradiation. *J. Phys. Chem. C* **2010**, *114*, 1963–1968. [CrossRef]

35. Li, H.L.; Li, T.D.; Liu, H.X.; Huang, B.B.; Zhang, Q. Hierarchical flower-like nanostructures of anatase TiO$_2$ nanosheets dominated by {001} facets. *J. Alloy Compd.* **2016**, *657*. [CrossRef]

36. Xu, L.; Ji, X.; Jiang, J.G.; Han, L.; Che, S.; Wu, P. Intergrown zeolite MWW polymorphs prepared by the rapid dissolution–recrystallization route. *Chem. Mater.* **2015**, *27*, 7852–7860. [CrossRef]

37. Yang, F.L.; Liu, Y.F.; Lu, Y.; Song, F.; Qian, H.; Yuan, Z. Citric acid-mediated microwave-assisted hydrothermal synthesis and luminescence property of NaSm(MoO$_4$)$_2$ submicro-crystals. *J. Mater. Sci.* **2015**, *26*, 8595–8602. [CrossRef]

38. Yu, J.G.; Jin, J.; Cheng, B.; Jaroniec, M. A noble metal-free reduced graphene oxide–CdS nanorod composite for the enhanced visible-light photocatalytic reduction of CO$_2$ to solar fuel. *J. Mater. Chem. A* **2014**, *2*, 3407–3416. [CrossRef]

39. Sing, K.S.W.; Everett, D.H.; Haul, R.A.W.; Moscou, L.; Pierotti, R.A.; Rouquerol, J.; Siemieniewska, T. Reporting physisorption data for gas/solid systems with special reference to the determination ofsurface area and porosity. *Pure Appl. Chem.* **1985**, *57*, 603–619. [CrossRef]

40. Jin, J.; Yu, J.; Liu, G.; Wong, P.K. Single crystal CdS nanowires with high visible-light photocatalytic H$_2$-production performance. *J. Mater. Chem. A* **2013**, *1*, 10927–10934. [CrossRef]

41. Min, Y.L.; He, G.Q.; Xu, Q.J.; Chen, Y.C. Dual-functional MoS_2 sheet-modified CdS branch-like heterostructures with enhanced photostability and photocatalytic activity. *J. Mater. Chem. A* **2014**, *2*, 2578–2584. [CrossRef]

42. Xu, Y.X.; Bai, H.; Lu, G.W.; Li, C.; Shi, G.Q. Flexible graphene films via the filtration of water-soluble noncovalent functionalized graphene sheets. *J. Am. Chem. Soc.* **2008**, *130*, 5856–5857. [CrossRef] [PubMed]

Sample Availability: Samples of MoS_2 QDs and MoS_2/CdS are available from the authors.